Computers in Biology and Medicine 110 (2019) 79–92

Contents lists available at ScienceDirect

Computers in Biology and Medicine

journal homepage: www.elsevier.com/locate/compbiomed

The influence of hematocrit on the hemodynamics of artificial heart valve using fluid-structure interaction analysis

Han Hung Yeh[a,b], Oleksandr Barannyk[c], Dana Grecov[a,b,*], Peter Oshkai[d]

[a] Department of Mechanical Engineering, University of British Columbia, 2054-6250, Applied Science Lane, Vancouver, BC, V6T 1Z4, Canada
[b] School of Biomedical Engineering, University of British Columbia, 2222 Health Sciences Mall, Vancouver, BC, V6T 1Z3, Canada
[c] Baylis Medical Company, 2775, Matheson Blvd. East, Mississauga, ON, L4W 4P7, Canada
[d] Department of Mechanical Engineering, University of Victoria, PO Box 1700 STN CSC, Victoria, BC, V8W 2Y2, Canada

ARTICLE INFO

Keywords:
Bileaflet mechanical heart valve
Hemodynamics
Fluid-structure interaction
Hematocrit
Particle image velocimetry

ABSTRACT

Patients with severe aortic stenosis could regain the proper hemodynamic performance and cardiovascular output by restoring the diseased aortic valve with an artificial heart valve replacement. However, given the uniqueness of each patient, the hemodynamic improvements after an aortic valve replacement could vary. The biomechanical and hemodynamical parameters can be influenced by some major factors including the patient's blood pressure and hematocrit. Therefore, the objective of this study is to analyze the hemodynamics and valve mechanics of a bileaflet mechanical heart valve and investigate the hemorheological characteristics under the change of hematocrit. The fully coupled fluid-structure interaction (FSI) approach was used to model the hemodynamics and valve dynamics. Particle image velocimetry (PIV) experiments were conducted with *in vitro* benchtop model using ViVitro Pulse Duplicator to verify and validate the FSI models. The current numerical analysis revealed the hematocrit influenced the shear stress distributions over a cardiac cycle. The structural stresses in the mechanical valve were also affected by the distributions of the shear stress in the blood flow. Parameter dependencies found in the current study indicate that the hematocrit is influential when conducting patient-specific modelling of prosthetic heart valves.

1. Introduction

Heart valve stenosis is a disease associated with the narrowing of a heart valve, which leads to the decrease in valve orifice area and might potentially lead to fatal complications. Subjected to the highest mechanical loads, most disorders of the heart initiate within the left ventricle, which is regulated by the mitral and the aortic valves influencing the inflow and the outflow conditions, respectively [1]. The most commonly affected heart valves in a diseased heart are the mitral and the aortic valves responsible for 34% and 44% of morbidity, respectively [2,3]. Based on the recent American Heart Association and American College of Cardiology guideline for managing patients with heart valve disease, the mechanical heart valve is considered for patients under 50 years old without the constraints of receiving anticoagulation [4]. The decision for a mechanical or bioprosthetic valve for patients between 50 and 70 years old would be patient-depended due to the devices' own disadvantages [4,5].

Computational fluid dynamics (CFD) that utilizes the concepts of fluid-structure interactions (FSI) has been used for the investigations of cardiovascular diseases including those related to aneurysms and heart valves [6–9]. While CFD study can be used to study bileaflet mechanical heart valve (BMHV) with prescribed particle image velocimetry (PIV)-measured leaflet motion [10] and localized flow features in a patient-specific aorta [11], the FSI method can provide further analysis in the simulation of heart valve where the blood flow would influence leaflet motion and vice versa. Early FSI works related to the current study include a 2D hemodynamic investigation of an artificial heart valve with subaortic stenosis [12], an FSI model using a 2D dynamic mesh with experimental validation [13], a 3D FSI BMHV simulation over a range of Reynolds numbers [14], as well as 3D symmetric BMHV analysis [15]. Recent BMHV modelling in 3D using FSI method was achieved by several groups including the integration of anatomical ascending aorta [16], assessing thrombosis potential with shear stress [17], and the assessment of BMHV hemodynamics [18,19]. Additionally, an FSI study focusing on BMHV's implant angle suggested angle dependency on the blood flow [20], and the use of the lattice-

* Corresponding author. Department of Mechanical Engineering, University of British Columbia, 2054-6250, Applied Science Lane, Vancouver, BC, V6T 1Z4, Canada.
E-mail address: dgrecov@mail.ubc.ca (D. Grecov).

https://doi.org/10.1016/j.compbiomed.2019.05.003
Received 27 April 2019; Accepted 1 May 2019

Boltzmann method could provide detail hemodynamic analysis [8,21]. The accuracy of the FSI method in a 3D BMHV simulation was validated by Guivier-Curien et al., where their Fluent FSI simulation was compared with PIV measurements [22].

The effects of the non-Newtonian behaviour of the blood on BMHVs have also been investigated. Recently, De Vita et al. presented an FSI simulation with BMHV focusing on hemolysis using the Carreau-Yasuda model [23]. They concluded that the prediction of hemolysis would be depended on the fluid model. Additionally, Hanafizadeh et al. investigated flow in coronary arteries during diastole with an aorta geometry derived from patient medical images using CFD with a focus on the influence of the non-Newtonian model on the wall shear stress and the near-hinge microflow [24]. Doost et al. conducted a CFD-based evaluation of the left ventricular flow using patient-specific geometry with multiple rheological models, including Newtonian, Carreau, Casson Cross, Power Law, and K-L model, and concluded that the usage of the non-Newtonian models would significantly affect the results of the CFD analysis [25]. Current FDA (Food and Drug Administration) guideline on CFD simulations for a medical device does not specify the requirement for the hemorheological model; however, incorporate a more realistic non-Newtonian rheological model in the analysis could provide a better prediction in medical device evaluation [26].

To consider the blood's non-Newtonian behaviour in cardiovascular modelling, the Carreau model was most frequently used in the literature [23–25]. A comparative CFD study using different non-Newtonian models on a 3D healthy volunteer aorta from a computerized tomography scan concluded that the Newtonian model underestimated the wall shear stress with a noticeable difference from the Cross model [27]. However, when considering patient-specific modelling, the Carreau model could not be easily adapted, as the rheological parameters used in the model do not have direct clinical counterparts. The Quemada model [28], on the other hand, has an additional parameter that uses the hematocrit to determine the behaviour of the blood. Marcinkowska-Gapińska et al. conducted a rheological investigation on post-infarction patients under Aspirin and free of anticoagulants [29]. Their data were fitted with three non-Newtonian models (Casson, Ree-Eyring, and Quemada) and concluded that the Quemada model was the most suitable [29]. The Quemada model has also been implemented to study the hemodynamics of abdominal aortic aneurysm [30,31] and diseased thoracic aorta [32].

There are several important issues remained unresolved even though BMHV has been investigated during the past two decades. A strong connection between the investigation of BMHV evaluation and patient management is still required. The use of the hematocrit as a patient-specific parameter in modelling blood for medical devices could be the first step for closing the gap. Although one's hematocrit would temporally increase during exercise due to the decrease in plasma volume, the elevated hematocrit recovered after 30 min of resting [33]. Therefore, the objective of the current study is to analyze the hemodynamics of a bileaflet mechanical heart valve (BMHV) and investigate the hemorheological characteristics due to the change in hematocrit using a fully coupled FSI approach.

2. Methodology

2.1. Experimental system

To validate the numerical model, phase-resolved velocity measurements under physiologically relevant test conditions were conducted. A commercially available, 23 mm BMHV with a tissue annulus diameter/internal diameter (TAD/ID) of 18.5 mm (Fig. 1), was used as the test model. Fig. 2 shows the schematics of the experimental apparatus that allowed investigation of the heart valve in the aortic configuration. The pulsatile flow was generated using a ViVitro pulse duplicator, which is a heart model designed for assessing the performance and function of prosthetic heart valves under simulated cardiac

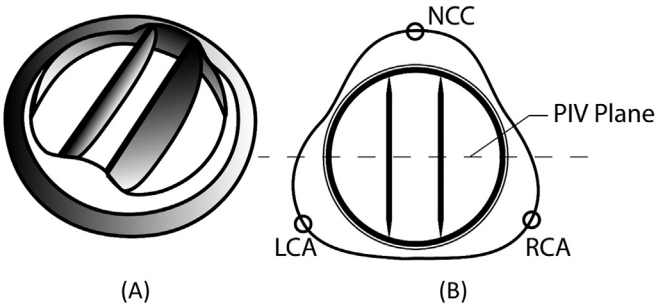

Fig. 1. Schematic of bileaflet valve (*left A*) and the orientation of the valve (*right B*) with respect to the left coronary artery (LCA), the right coronary artery (RCA) and the noncoronary cusp (NCC) (Note that the PIV Data Acquisition Plane is shown with dashed lines).

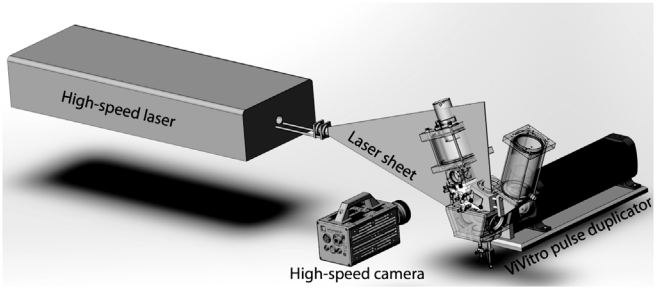

Fig. 2. Schematic illustrating DPIV test set-up used in the current experiment (Image courtesy of ViVitro Labs Inc.).

conditions. The pulse duplicator was powered by a piston-in-cylinder pump driven by a motor connected to the ViViTest data acquisition and control unit that controlled the pump. This setup allowed for the generation of various ventricular pressure waveforms and beat rates while generating physiological pressures and flow regimes in the vicinity of the valve.

To simulate the physiological flow conditions, an acrylic test chamber, that represented a simplified model of the ascending section of a human aorta, was fabricated. This experimental set up allowed visualization of the flow upstream and downstream of the heart valve in the aortic position. The geometry and the dimensions of the acrylic chamber are shown in Fig. 3. The internal cavity of the test chamber also included sinuses of Valsalva, so that cusp dynamics can be simulated.

Experiments were conducted at nominal conditions in accordance with ISO 5840–2:2015 [34], at a simulated heart rate of 70 beats/min (BPM) that corresponds to a cardiac cycle with a period T = 860 ms, the target cardiac output of 5.5 l/min, the mean aortic pressure of 100 mmHg. The duration of the systolic phase was approximately 35% of the cardiac cycle period. The tests were conducted at a temperature of 37 °C. The working fluid, in the current experiment, was a mixture of glycerin and water in the ratio of 40:60 that had a dynamic viscosity of 3 mPa s and a specific gravity of 1.1 at 37 °C.

Optical distortions introduced by the curvature of certain elements of the test chamber were corrected in post-processing with the help of Davis 8.1.3 software (LaVision Inc.). A square grid with a mesh element size of 1 mm was positioned in the plane of interest of the test section that contained the working fluid. An image of the grid was subsequently subjected to a polynomial calibration fit that addressed both spherical and cylindrical distortions. The areas of remaining local distortion were removed by an algorithmic mask, and the velocity vectors in these areas were interpolated using available neighbouring data points.

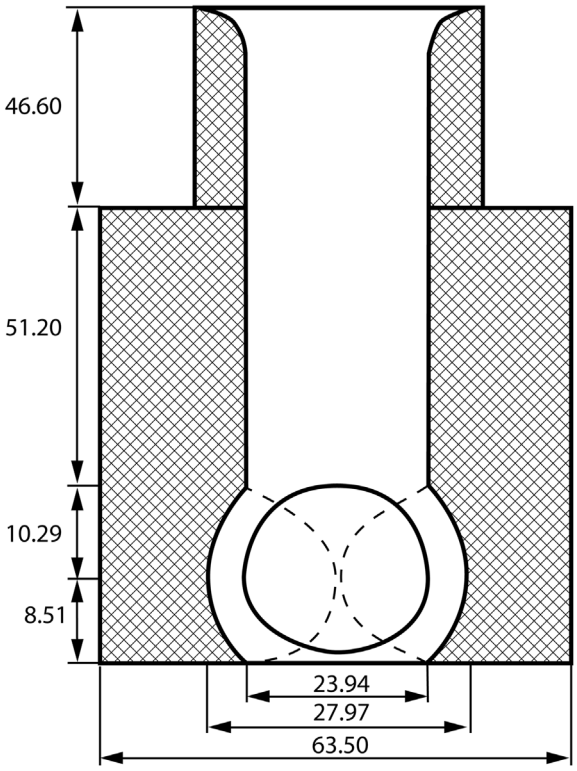

Fig. 3. Acrylic test chamber with geometrical specifications (dimensions in mm).

2.2. Time-resolved PIV

The technique of time-resolved PIV was implemented to collect flow velocity data in the vicinity of the bileaflet valve, which is shown in Fig. 1. Among the advantages of the PIV technique is its non-intrusiveness and capability of delivering data with high spatial and temporal resolution. The PIV system included an Nd:YLF dual cavity laser (power output of 22.5 mJ/pulse at 1 kHz, wavelength of 527 nm).

The flow was seeded with silver-coated hollow glass spheres with a mean diameter of 14 μm and specific gravity of 1.3, relative to water, which acted as flow tracers. The Stokes number of the tracer particles was equal to 0.7×10^{-3}, which indicated that the particles were sufficiently small to accurately follow the flow [35]. The images of the tracers were recorded using a Photron Complementary Metal Oxide Semiconductor (CMOS) camera with a sensor that consisted of 1024 × 1024 pixels, which was oriented parallel to the data acquisition plane shown in Fig. 1. The physical resolution of the flow images was equal to 17 μm/pixel, with the size of the tracer particles of 2 pixels. The field of view of the camera corresponded to the area of 70 mm × 30 mm, which extended 1.5D upstream and 3D downstream of the valve. The origin (X = 0 mm, Y = 0 mm) corresponded to the center of the outflow area of the gasket holding the valve.

Images were collected in the central plane, which is defined in Fig. 1 and in the double-frame double-exposure mode, where for each pair of consecutive frames acquired by the camera, the pulse from the first laser cavity provided illumination for the first frame in the pair, and the pulse from the second laser cavity illuminated the second frame. This data acquisition regime resulted in the sampling rate (of the cross-correlated image pairs) of 100 Hz and the time interval between the frames in a pair of 500 μsec. The PIV data was acquired at five representative phases of the cardiac cycle, indicated by black circles in Fig. 4. These phases correspond to the opening acceleration phase (t/T = 0.05), the peak systolic phase (t/T = 0.13), the closing phase (t/T = 0.29), and the leakage phase (t/T = 0.69). Here t denotes time and

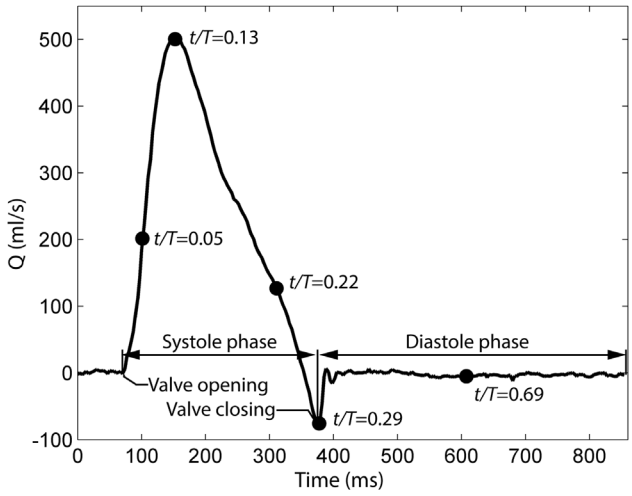

Fig. 4. Variation of the flow rate as a function of time during a typical cardiac cycle (black circles correspond to the phases of the cardiac cycle, at which PIV data were obtained).

T = 860 ms is the period of the simulated cardiac cycle.

The collected images were processed by the Davis 8.1.3 software using a multipass cross-correlation algorithm. The initial pass involved 64 pixels × 64 pixels interrogation windows with a 50% overlap between the adjacent windows in both X- and Y-directions. The final pass involved 16 pixels × 16 pixels interrogation windows with a 50% overlap in both directions. The resulting spacing of the velocity vectors was equal to 8 pixels × 8 pixels, which corresponded to the resolution of 7 vectors/mm in the physical flow domain. The typical error in the calculated particle displacement for PIV correlation algorithms of this kind is of the order of 0.1 pixels [36,37]. There were also measurement artifacts near wall boundary resulting in decrease experimental measurement certainties. The sources of error could potentially result from insufficient treatment in data collection near the wall [39] or a bigger seeding particle sized used in the current study [40]. Based on the 16 × 16 pixel window used for correlation, a conservative estimate of 5% error excluding the wall in true displacement can be assumed [38]. Therefore, the data near the wall boundary was excluded during numerical model validation.

2.3. Governing equations

The blood flow was modelled by the incompressible Navier-Stokes equations with the equations for fluid continuity (Eq (1)) and momentum conservation (Eq (2)) shown below. Flow is assumed to be within the laminar regime as the Reynolds number for the current study is less than the critical Reynolds number under oscillatory flow based on the criterion by Ohmi and Iguchi [41]. The laminar flow assumptions also agree with various studies in the analysis of BMHV [16–18]. Additionally, the blood flow is assumed to be incompressible with negligible gravitational force. The interactions between blood flow and valve leaflet were computed with the coupling equation (Eq (3)). Cauchy stress tensor, **σ**, was calculated based on the pressure and the viscous terms from the momentum equations from Navier-Stokes. Finally, the von Mises stress used to evaluate the leaflet stress is calculated based on Eq (4).

$$\nabla \cdot \boldsymbol{V} = 0 \tag{1}$$

$$\rho \frac{D\boldsymbol{V}}{Dt} = \nabla \cdot (-P\boldsymbol{I} + \boldsymbol{\tau}), \tag{2}$$

$$\boldsymbol{\sigma} \cdot n = (-P\boldsymbol{I} + \boldsymbol{\tau}) \cdot n \tag{3}$$

$$\sigma_{vM} = \sqrt{3\left(\frac{1}{2}tr(\boldsymbol{\sigma}^2) - \frac{1}{3}tr(\boldsymbol{\sigma})^2\right)} \quad (4)$$

where **V** is the fluid velocity, ρ is the fluid density, P is the pressure, **I** is the identity tensor, $\boldsymbol{\tau}$ is the viscous stress tensor, n is the unit normal vector, and σ_{vM} is the von Mises stress.

The Quemada model was used to account for the non-Newtonian shear thinning behaviour of the blood's viscosity under the change of the hematocrit, as shown in Eq (5) [28].

$$\mu = \frac{\mu_{plasma}}{\left(1 - \frac{Htc \cdot k_{eq}}{2}\right)^2} \text{ and } k_{eq} = \frac{k_0 + k_\infty \cdot \sqrt{\dot{\gamma}/\dot{\gamma}_c}}{1 + \sqrt{\dot{\gamma}/\dot{\gamma}_c}} \quad (5)$$

where the μ_{plasma} is the viscosity of blood plasma, Htc is the hematocrit, k_0 and k_∞ are the maximum volume fraction at zero and infinite shear rates, $\dot{\gamma}$ is the shear rate, and $\dot{\gamma}_c$ is the critical shear rate for erythrocytes agglomeration.

The rheological parameters (μ_{plasma}, $\dot{\gamma}_c$, k_0, and k_∞) were taken from the study conducted by Marcinkowska-Gapińska et al. for the blood rheology measured at body temperature for a patient without anticoagulation intake for a week prior to the measurements [29]. Although these parameters could also be influenced by the hematocrit [42], the four rheological parameters were kept constant for current study with μ_{plasma}, $\dot{\gamma}_c$, k_0, and k_∞ equal to 1.28 mPa s, 4.2 s^{-1}, 4.01, and 1.77, respectively [29]. Based on Eq (4), the shear rate-dependent Quemada viscosity for a wide range of shear rates is plotted in Fig. 5. To visualize better the shear thinning behaviour at high shear rates, the hollow lines on the right-hand side of Fig. 5 represent the viscosity above 100 s^{-1} with the magnitude in Pa-s labeled on the right vertical axis, as indicated by the black arrow. The degree of shear thinning changes dramatically for shear rates below 10 s^{-1}, where a higher hematocrit resulted in a significantly increase in viscosity at a lower shear rate region.

2.4. Computational method

The current numerical models were constructed using COMSOL Multiphysics (V5.2a, Stockholm, Sweden) with parallel sparse direct solver MUMPS (MUltifrontal Massively Parallel Sparse direct Solver). The numerical setup was inherited from the experiment, including the geometrical specifications of the acrylic chamber and the applied physiological pressures. The fully-coupled, 2-way FSI models were built based on the approach from our previous study [43,44], where ALE method was used to calculate the displacement of the valve leaflet under physiological blood pressure. A computational model

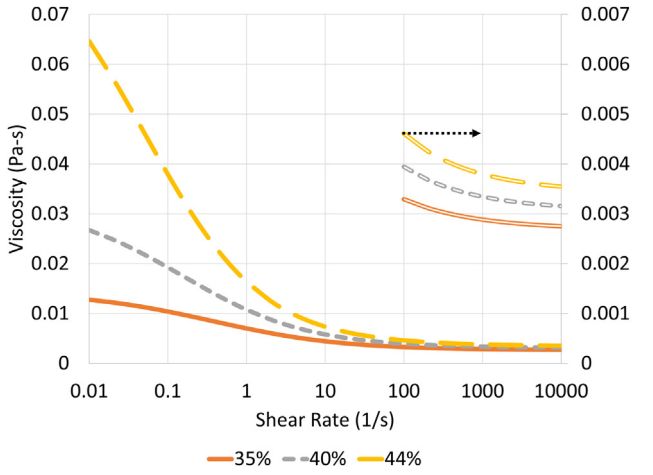

Fig. 5. Viscosity predicted by the Quemada model as a function of shear rate for different hematocrits (hollow lines refer to viscosity value after 100 s^{-1} using a secondary axis on the right).

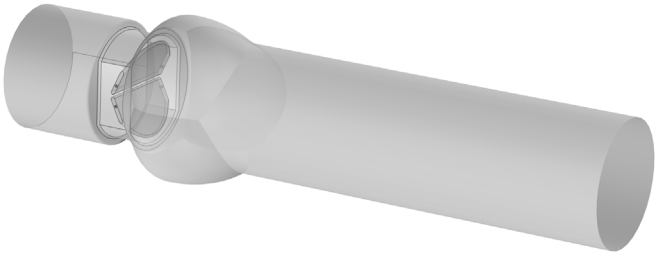

Fig. 6. Computational domain corresponding to the experimental geometry.

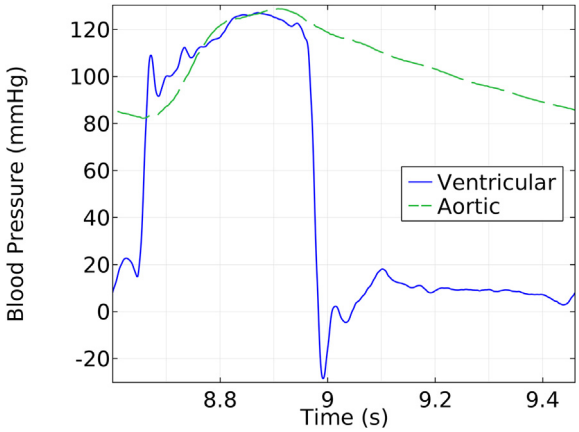

Fig. 7. Physiological blood pressure profiles for the ventricular (inlet) and aortic (outlet) boundary.

representing the benchtop experimental setup was built to validate the numerical method with the same geometrical and material properties. The BMHV had a diameter of 23 mm, a leaflet thickness of 0.78 mm, a length of 10.27 mm and a free rotation angle ranging from 25° to 85°. The valve leaflets were assumed to be isotropic linear elastic with Young's modulus of 30 GPa, Poisson's ratio of 0.3, and a density of 2116 kg/m^3, similar to the study by Choi and Kim [18]. The computational domain is shown in Fig. 6. At the inlet and the outlet boundaries, the physiological pressure profiles were applied as same as in the experimental setup, as shown in Fig. 7. To account for the solution instability due to initial conditions, a total of 8.6 s (ten cardiac cycles) of the diastolic pressure was applied. The fluid-structure interface was specified along with the BMHV surface. The free rotation condition was applied independently to the four valve hinges with angular constraints at 25° to 85° ± 0.001°. To avoid reaching solution singularity and because of the variations in geometrical scales, the butterfly hinges of an actual BMHV were simplified as simple pin hinges without fluid flow in between. The effect of these geometrical simplifications on the hemodynamics and valve leaflets stress distributions was assumed to be minimal.

The computation for the fluid and structure domain was fully coupled with a relative error less than 1e-3. Mesh convergence study was conducted to verify that the solutions were independent of the discretization of the computational domain. Both tetrahedral and brick types of mesh elements were used to account for a computational boundary and maximize computational efficiency. The average blood flow velocity magnitude along the centreline of the computational domain was analyzed for the first ten cardiac cycles. A convergence was concluded when the difference between the velocities was within 2% for all the time instances throughout the cardiac cycle. Temporal convergence was confirmed at the seventh cardiac cycle.

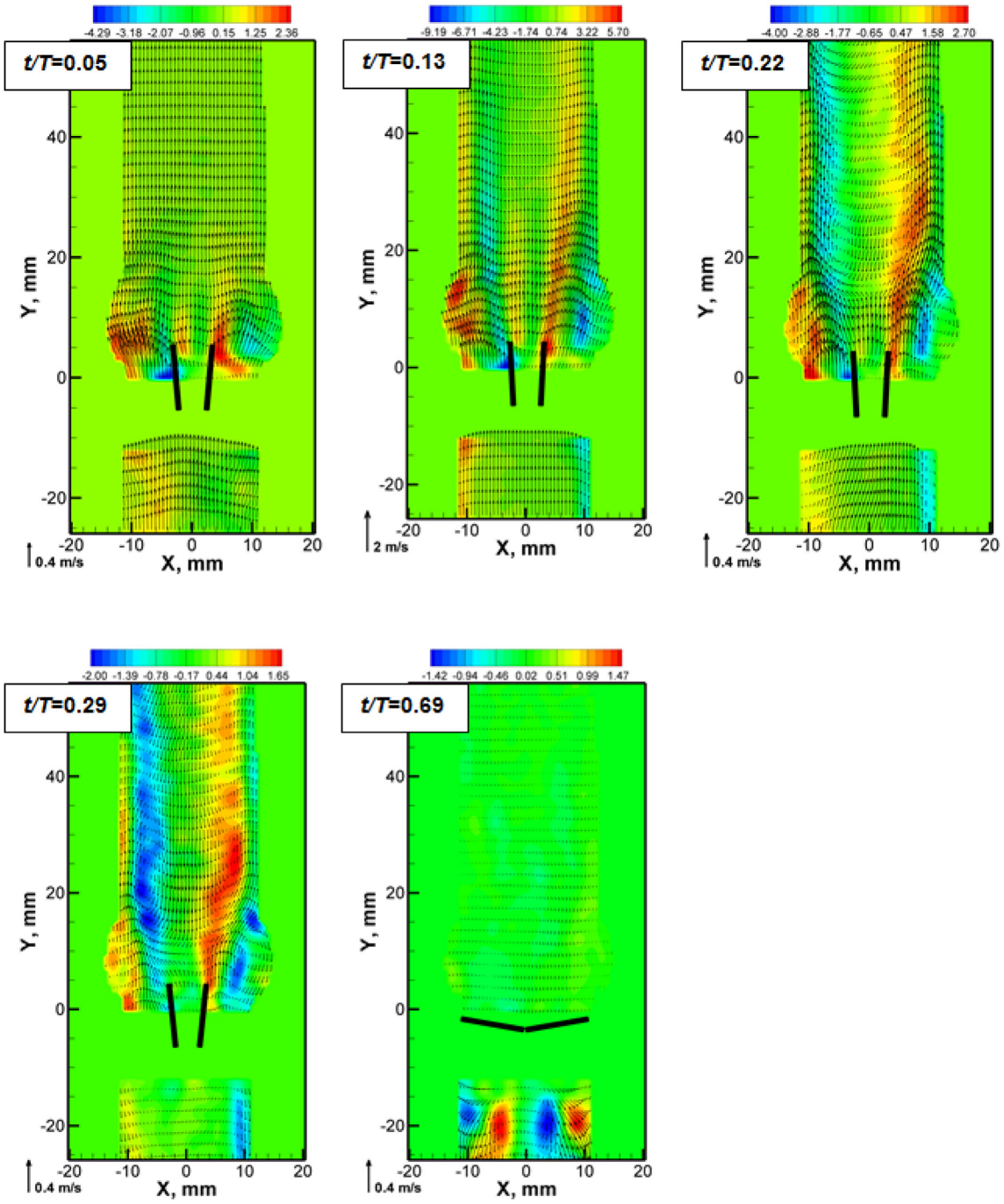

Fig. 8. Experimental velocity vector fields and contours of viscous shear stress (dPa) at several instances during the systolic phase of the cardiac cycle for the case of the bileaflet valve.

3. Results

3.1. PIV experiments

In this section, the overall flow characteristics of the BMHV are illustrated at five representative phases of the cardiac cycle, and patterns of ensemble-averaged velocity and viscous shear stress are discussed.

In Fig. 8, one can see that as the two leaflets were forced open by incoming accelerating flow, a typical triple orifice jet configuration was created. The peak velocities for the left, the central, and the right jets in the plots of Fig. 8 were 0.88 m/s, 0.77 m/s, and 0.89 m/s, respectively, at t/T = 0.05, which corresponds to the flow acceleration phase. Each of the peripheral orifice jets was characterized by two shear layers: the outer shear layer that was separated from the valve housing and the inner shear layer that originated from the tip of the leaflet. The orientation of the peripheral jets with respect to the central axis of the model of the aorta was strongly influenced by the opening angle of the valve leaflets, which was equal to 71° with respect to the horizontal axis. During the acceleration phase, the developing peripheral jets were inclined towards the aortic sinuses. The velocity patterns indicate that the outer shear layers extended into the sinuses. At the phase corresponding to the maximum forward flow through the valve (t/T = 0.13), the velocity magnitude in the peripheral jets reached 1.3 m/s at Y = 20 mm. The opening angle at this phase was 87° with respect to the horizontal axis.

During the flow deceleration phase, at t/T = 0.22, the valve's

opening angle decreased to 84° which lead to the decrease of maximum velocity in the peripheral jets to 0.4 m/s. At the same time the central jet structure disappeared, as the closing valve leaflets restricted the available flow area in the center of the valve. A well-defined recirculation zone was formed near the centerline of the aorta, between the two peripheral jets and immediately downstream of the aortic sinuses. These flow patterns are in agreement with the flow structure reported in Ref. [10].

During the closing phase, at t/T = 0.29, two recirculation zones were observed on the aortic root side of the valve. The orientation of the recirculation zones was highly influenced by the presence of the leaflets and it was directed towards the valve along the centerline of the aorta, and away from the valve along the aortic walls. On the ventricle side of the valve, regurgitation jets were observed. The jets originated from the small gap between the closing leaflets (eventually completely closed). During the diastole phase, at t/T = 0.69, BMHV exhibited flow regurgitation, or leakage, which manifested as jets of fluid directed into the ventricle. In particular, two regurgitation jets were produced by the openings around the hinges of the leaflets. The jets were oriented outwards from the centerline of the valve and had the characteristic velocity magnitude of 0.2 m/s. BMHV was intentionally designed to produce strong regurgitant jets through its hinges in order to avoid the potential formation of thrombi in and around the hinges [45].

3.2. Numerical results

To validate the FSI model with the PIV experiment, the flow velocity along the PIV data acquisition plane was analyzed. Both the numerical and the experimental models were under the same operating conditions including the matching geometry and Newtonian fluid properties. The locations for validating the blood flow velocities were chosen to be within the aortic sinus at the widest cross-section downstream from the BMHV. These locations corresponded to be approximately at 9 mm, 12 mm and 15 mm downstream, measured from the base of BMHV. The velocity profiles at the validating locations were plotted at peak systole of 8.75s and end systole of 8.80s for the comparison between the numerical and the experimental models, as shown in Fig. 9. The overall difference in flow velocity distributions at three locations and two time-steps was 6.1%, ranging between −6.5% (8.80s, 9 mm) to 16.2% (8.75s, 15 mm). The absolute difference between the six instances evaluated was 14.6%. Due to the influence of optical distortion from the acrylic chamber, the PIV accuracy for near-wall measurements was reduced; therefore, the velocity distributions were validated slightly away from the acrylic wall approximately 3 mm from each side. The inaccuracy and uncertainties from the measurement arose mainly from the optical artifacts and occurred near the wall. The measurement could have been improved by refining the interrogation area similar to the work by Nguyen et al. [39]. Additional qualitative validations against literature published PIV measurements were therefore conducted in order to provide further support to the existing numerical model. The simulated peak systolic flow distributions within the aortic sinus close to the wall were in qualitative agreement with previous study conducted by Li et al. [40]. Furthermore, the leaflet dynamics was in close agreement with the simulated results by Choi and Kim with similar leaflet opening durations and leaflet rebound characteristics [18]. It was therefore concluded that our 3D FSI model was an overall representation of the experimental setup with qualitative validation from literature for flow near the wall boundary.

3.2.1. BMHV hemodynamics

The velocity contours at the central cross-section of the BMHV for the cases with 35% Htc., 40% Htc. and 44% Htc under systolic and diastolic conditions are shown in Fig. 10(a)-(f). The results at the peak of systolic phase (Fig. 10(a),(c),(e)) and the end of the diastolic phase (Fig. 10(b),(d),(f)) were presented for each hematocrit value. In general, all three scenarios yielded similar velocity distributions both in velocity magnitude and direction. The inclusion of non-Newtonian modelling showed minor variations in the distributions of the vortices within the aortic sinus at systole and behind the valve leaflet at diastole due to the blood's shear-thinning behaviour. Additionally, the

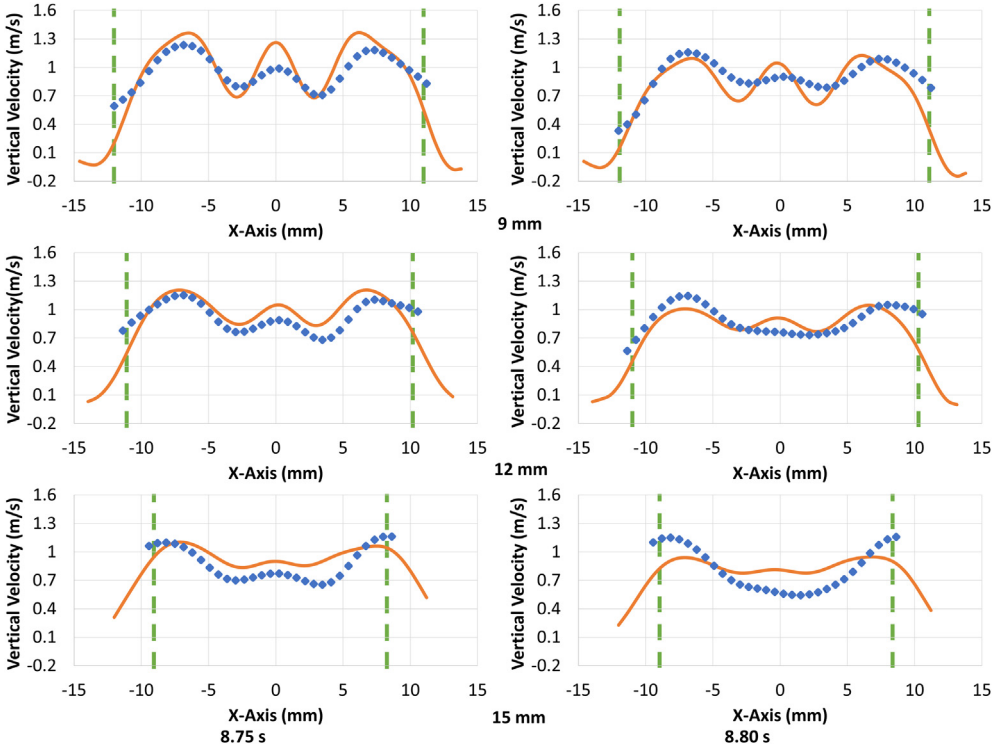

Fig. 9. Velocity profile validation at 9 mm downstream from BMHV at peak systolic phase with the dotted and the solid line representing the experimental data and the numerical result, respectively (the long dash lines represented the locations 3 mm away from the wall).

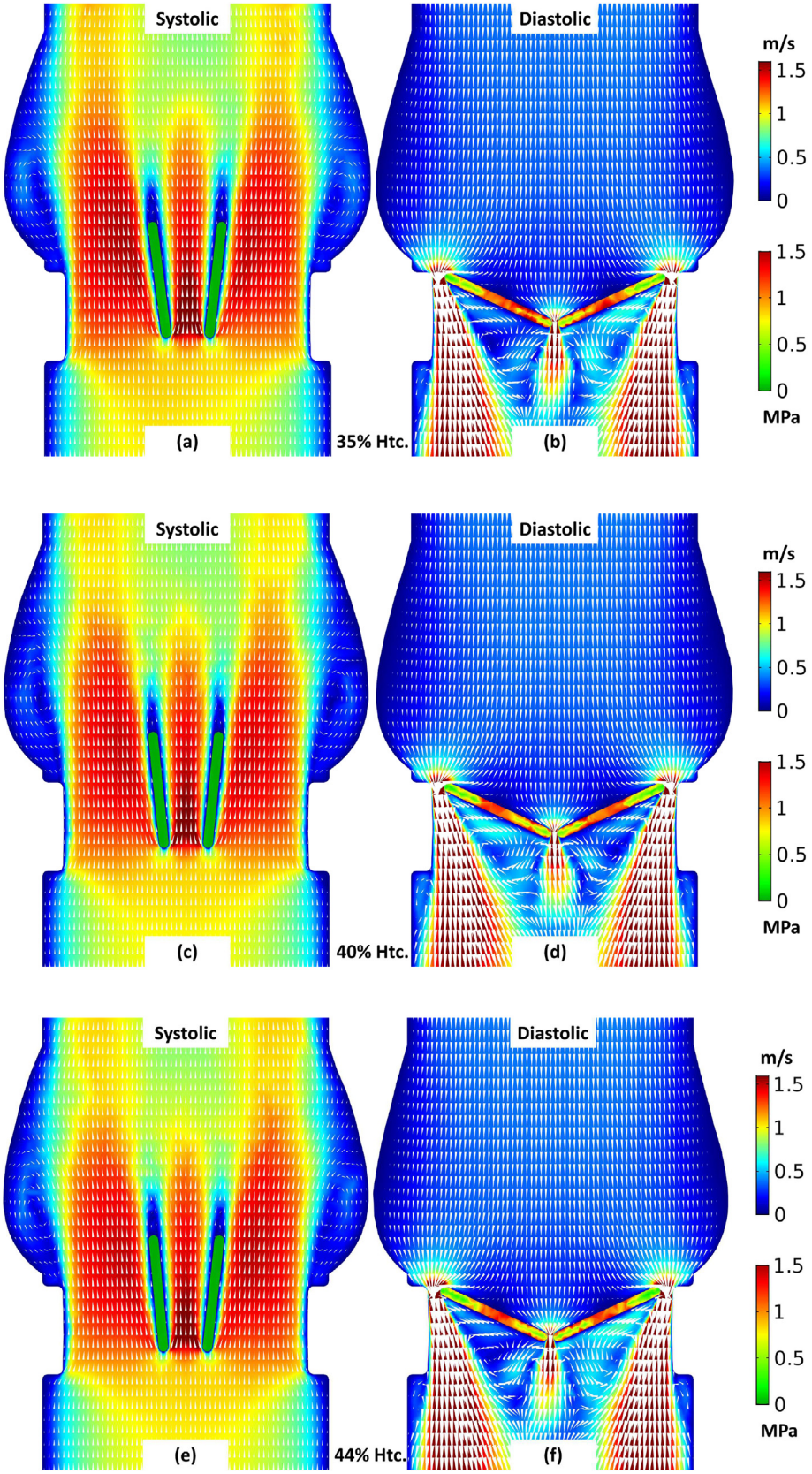

Fig. 10. Computed velocity vector fields and contours of velocity magnitude at the central cross-sectional plane for peak systole and end diastole under different hematocrit conditions.

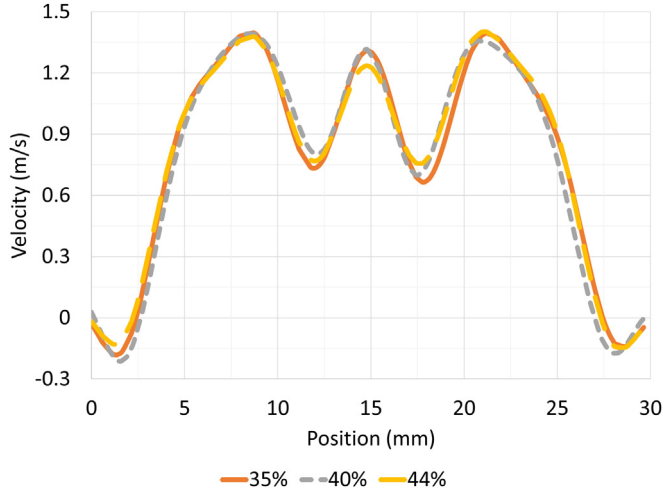

Fig. 11. Peak Systolic velocity profiles at 9 mm downstream away from BMHV with different hematocrit of 35%, 40%, and 44%.

numerical models retained additional flow features such as re-circulatory flow, or the washout characteristics, within the aortic sinus at the systolic phase and behind the valve leaflet at the diastolic phase. Both flow recirculation at systole and diastole were not visible in the experimental result due to the PIV field of view obstruction by the valve housing.

The BMHV generated the distinctive three-jet flow when the valve fully opened. The velocity profiles (Fig. 11) indicated similarity for all three scenarios at 9 mm downstream or the location where experimental validation was conducted. Blood was ejected through BMHV with a maximum ejection velocity of 1.4 m/s at the sides while the recirculatory blood within aortic sinus had a reversed velocity just under 0.3 m/s for all cases.

Additionally, the 3D velocity vectors downstream the BMHV were plotted (Fig. 12) to present the spatial velocity distributions. While the 2D contours in Fig. 10 clearly mapped the distribution of the velocity jet, additional detail was revealed regarding the spatial orientation of the semilunar blood flow jets from the two sides of BMHV and the elliptical central jet. Flow recirculation due to the expansion of the aortic sinus was also observed at systole (Fig. 12(a),(c),(e)). At diastole (Fig. 12(b),(d),(f)), reversed leakage jets passed through the inter-valvular space of BMHV. The leaks were more from the sides than at the center of BMHV, represented by the higher leakage velocity. The instantaneous leakage velocity magnitude reached 4 m/s at the tip of the valve leaflet while the flow velocity slowly diminishing to approximately 1 m/s near the inlet boundary. Note that in both Figs. 10 and 13, the colour legend for blood flow velocity was intentionally capped at 1.6 m/s to better visualize the velocity distribution. Overall, the hematocrit did not influence the region with high flow velocity significantly, but there were differences in the recirculation regions with lower flow velocity. The flow distributions around the valve leaflets and vortices generations within the aortic sinus were similar to the PIV measurements discussed in Fig. 8.

3.2.2. Shear stress distribution

The maximum shear stress magnitude was analyzed and plotted in Fig. 13 for the simulated cardiac cycle. The maximum shear stress magnitudes from one cardiac cycle were computed as 1766 dPa, 1935 dPa, and 2698 dPa for 35%, 40%, and 44% Htc. respectively. During the systolic phase, when BMHV fully opened, the maximum magnitude of the shear stress ranged approximately between 60 dPa and 500 dPa. However, during the diastolic phase, when BMHV fully closed with reversed leakage flow, the maximum shear stress reached approximately 2700 dPa for the case with 44% Htc. All three scenarios had similar shear stress distribution in time, yet, maximum shear stresses were significantly lower for the hematocrit of 35% and 40% during the diastolic phase after valve closure.

For the individual component of the shear stress, all three shear stress component, XY, XZ, and YZ, were plotted in Fig. 14 for peak systole and Fig. 15 for end diastole. Again, the results for all three cases, 35% Htc. ((a)-(c)), 40% Htc. ((d)-(f)), 44% Htc. ((g)-(i)), were presented. The spatial distributions of shear stress were similar across all considered cases. During the systolic phase (Fig. 14), the shear stress in the XY direction ((a),(d),(g)) concentrated near the tip of valve leaflet while the shear stress in the XZ direction ((b),(e),(h)) concentrated around BMHV housing. The shear stress in the YZ direction ((c),(f),(i)) concentrated along the valve leaflet surface and BMHV housing. Focusing on the case where hematocrit was 35%, the shear stress in all three components were significantly less than the 44% Htc. case.

On the other hand, the shear stress distribution for the 40% Htc. case was similar, but with smaller magnitude than the 44% Htc. case. The shear stress results at diastole (Fig. 15) revealed that all three shear stress components concentrated at the leaflet tips and the valve housing. Similar to the systolic phase, the shear stress distributions were similar between the 40% Htc. and the 44% Htc. case with high shear stress less concentrated for the 35% Htc. case. Note again that in both Figs. 14 and 16, the colour legend for shear stress was intentionally capped at 50 dPa to visualize the shear stress distribution.

3.2.3. Valve leaflet dynamics

The motion for both BMHV's leaflets was plotted in Fig. 16(a) and (b) over one cardiac cycle. All three hematocrit cases predicted similar opening period, approximately 200 ms on average, during systolic phase; however, not all the cases had the same leaflet motions during the opening period. We define the opening period to be the time between the time when the leaflet first reached the maximum opening and the time when leaflet first closed. Specifically, the 40% Htc. case maintained maximum opening throughout the whole systolic phase whereas the 35% Htc. case started the closure immediately after the maximum opening at peak systole was reached. The 44% Htc. model had leaflet 2 (Fig. 16(b)) maintained at maximum opening while leaflet 1 (Fig. 16 (a)) showed slight instability in maintaining valve opening. The 3D views of valve leaflet revealed a concentrated distribution of the leaflet stress near valve leaflet hinges at valve closure (Fig. 12(b),(d),(f)). Additionally, the maximum Von Mises stress experienced by the leaflets under all cases were below 90 MPa at the time of leaflet closure, which can be seen in Fig. 10(b),(d),(f) under the cross-sectional plane. This confirmed the durability of a BMHV and its unlikeliness to fail due to simple mechanical stress.

4. Discussion

Since the value of the hematocrit is a readily accessible parameter from a blood test result during clinical evaluations, the integration of the Quemada model into the current FSI analysis on BMHV provided additional insights. Given that the Quemada model is a phenomenological model that characterizes the overall viscosity-shear rate relationship of a system with concentrated disperse particles, whole human blood rheological behaviour could be accounted for based on the hematocrits. The rheological parameters used in the Quemada model could vary over a wide range of hematocrit values; therefore, the current study only considers a narrow but normal range of hematocrits. By analyzing three hematocrit values within the normal range, the influences in the change of hematocrit due to physiological factors can be mapped. We observed an overall decrease in maximum shear stress with the decrease in hematocrit; however, the decrease in shear stress was not linear with respect to the decrease in hematocrit due to the difference in the degree of shear thinning for each hematocrit value. Although the general velocity distribution remained similar between each hematocrit case, the localized recirculatory flow within aortic

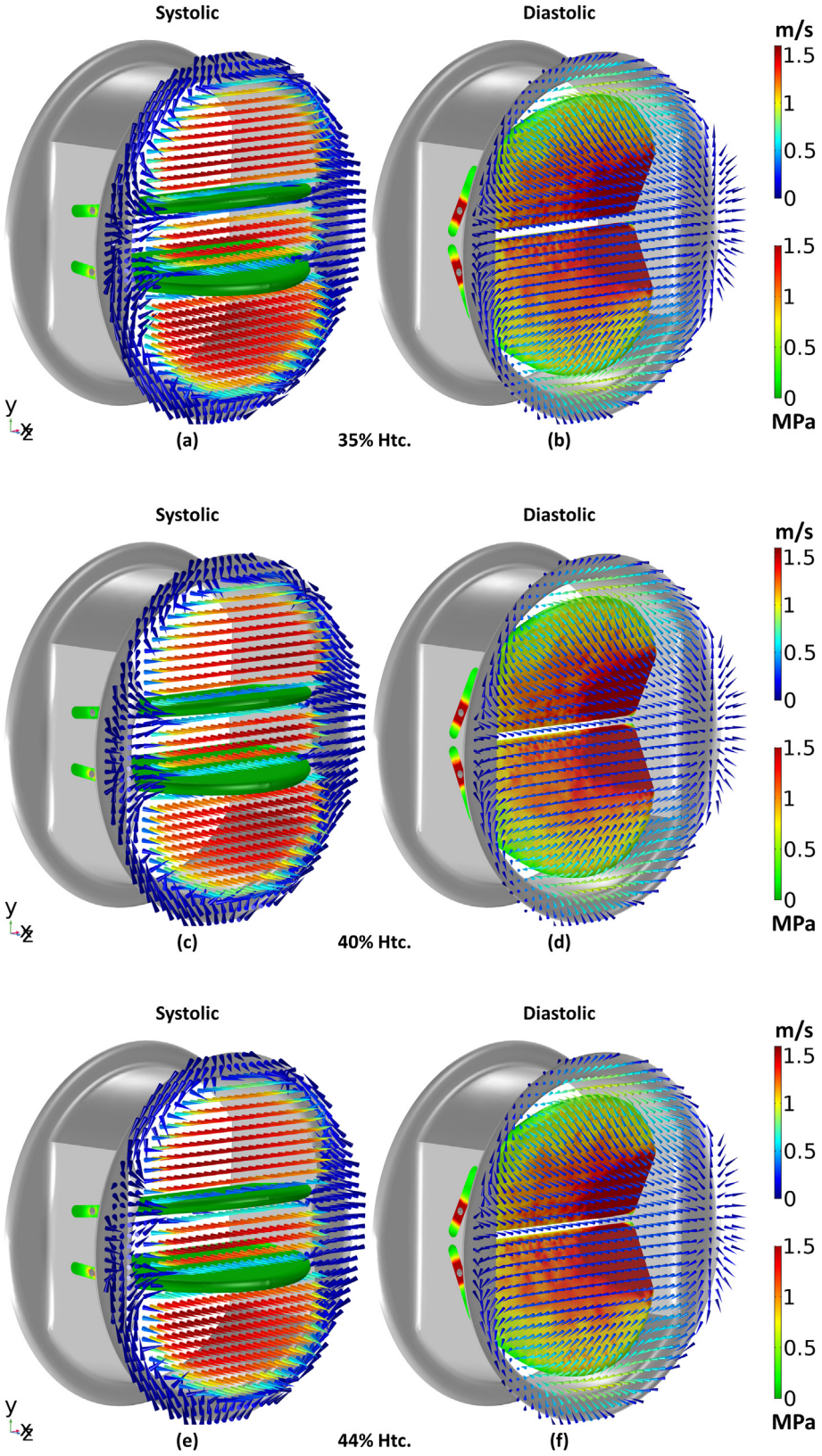

Fig. 12. 3D velocity vector plots downstream BMHV at peak systole and end diastole under different hematocrit conditions.

sinus near the wall had large variations when the hematocrit changed from 35% to 44% Htc. The detail comparisons between the cases with different hematocrit for each of the key physical parameter analyzed in the current study were summarized in Table 1.

4.1. The effect of hematocrit on BMHV hemodynamics

The maximum peak velocities were similar for all the cases; however, there were recirculatory/washout flow variations within the aortic sinus. Since the influence of shear rate on the blood's viscosity is

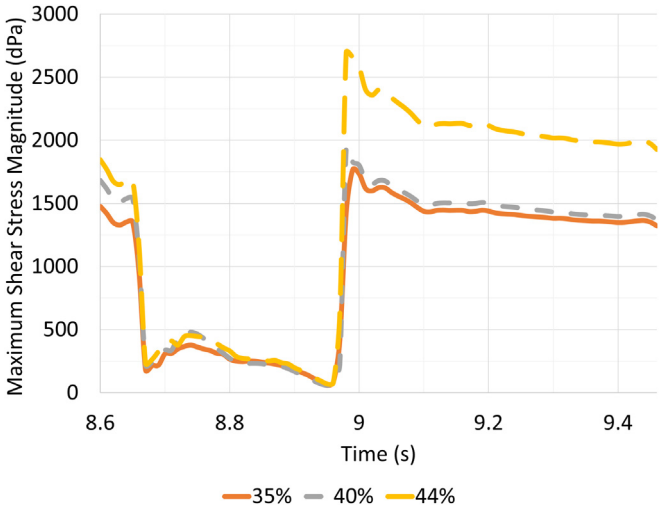

Fig. 13. Maximum shear stress magnitude within the computational domain with a different hematocrit of 35%, 40%, and 44%.

greater at low shear rate regime while the value of viscosity reaches a plateau at a shear rate of 100 s^{-1} and above, it is not a surprise that the difference in the hemodynamics would be found around the aortic sinus, where flow recirculation occurred. In our earlier work involving the characterization of the rheological properties of whole human blood, we observed a clear increase in the degree of the shear thinning of the blood's viscosity due to the increase of the hematocrit [46]. The viscosity could increase by approximately 32% at a low shear rate if the hematocrit was increased from 43% to 48%. Given that the fluid shear-thinning characteristics would affect the size of vortices generated as well as form secondary asymmetric flow [47], it would be important to consider the effect of these changes in rheological parameters in patient-specific hemodynamics modelling such as heart valves as the changes were not linear with respect with the change of hematocrit.

The maximum shear stress difference between the 35% Htc. case to the others were 9.5% (40% Htc.) and 52.7% (44% Htc.) as the result of a nonlinear change in the degree of shear thinning across the hematocrit values. Time-averaged shear stress (TASS) magnitudes had a similar value between 35% Htc. and 40% Htc. with a minor increase of 5.4%; however, there was a significant increase of 42.8% in TASS between 35% and 44% Htc. This result suggested that there was a greater influence from the 44% Htc. hemorheological model in TASS predictions. Since the difference in the viscosities at high shear rates was small and that the degree of shear thinning was increased nonlinearly at a low shear rate, our results suggested the importance of considering the hematocrit-depended rheology with performing hemodynamics evaluation in cardiovascular disease. Additionally, Fig. 13 identified instances where the maximum shear stress went above 1500 dPa for all models. Using a simple estimate for critical shear stress of 1500 dPa to evaluate cell damage [48], the current analysis would suggest blood cell damages due to BMHV regardless the value of hematocrit; therefore, anticoagulant would most likely be necessary for all cases. This result agreed with common practice for patients receiving an aortic valve replacement with a BMHV [49]. Given the wide variation in blood-induced shear stress across the three hematocrit values studied, which are considered as normal values, the patient's hematocrit might have significantly more importance during patient management.

4.2. The effect of hematocrit on BMHV leaflet motions

In general, the leaflet dynamics predicted in the current study were in good agreement with previous investigations [12,18]. However, due to the change in the hematocrit, the motion of BMHV leaflet was affected by these changes as shown in Figs. 16 and 17. There were variations in the valve opening phase for both valve leaflets given that the valve opened on averaged for 220 ms (35% Htc.), 217 ms (40% Htc.), and 193 ms (44% Htc.). Although the leaflet motions for 35% Htc. and 40% Htc. had a similar performance for both leaflets, the 44% Htc. case had an asymmetric leaflet dynamic resulting in 24.4% reduction in opening duration for one of its leaflets. The first leaflet for the 44% Htc. case had similar opening and closing time to the other hematocrit cases; however, the second leaflet for the 44% Htc. case reached the maximum opening at a later stage with a similar closing time (Fig. 17). This result indicated that the 44% Htc. case had the shortest opening period on average while the 35% Htc. case had incomplete leaflet openings (Fig. 16).

As the motion of the leaflet was simulated based on the forces exerted from fluid flow, these variations in the data set support the need to differentiate modelling properties, as intuitive as hemorheological profiles under different hematocrit, in order to conduct patient-specific simulation and diagnostic more carefully. The asymmetrical leaflet motions and the difference in valve opening duration due to the change of hematocrits further echoes the conclusion by Ternik that the change in the shear thinning behaviour of the fluid could result in flow asymmetry [47]. Additionally, severer leaflet rebounds were found during valve closure (Fig. 17(b)) with a rebound of 1.4° (44% Htc.) follow by the 0.8° (35% Htc.), and 0.1° (40% Htc.). These variations in leaflet motion due to the change in hematocrit, or the rheological behaviour of blood, warrant future investigations.

Finally, there were also some noticeable differences in Von Mises stress that the leaflets experienced. Similar to the maximum shear stress magnitude evaluated earlier, the 35% Htc. case had the lowest maximum Von Mises stress of 72.9 MPa evaluated but the 40% Htc. case had the highest value of 88.0 MPa, followed by 85.5 MPa (44% Htc.). The time-averaged difference in Von Mises stress was also calculated to be 11.7% (40% Htc.) and 17.3% (44% Htc.) with respect to the 35% Htc. baseline. Although there were differences in structure stress under current FSI investigation in BMHV, these differences in stress evaluation will be more influential for modelling involving biological tissue since the maximum stress in current BMHV would less likely cause simple mechanical failure given the small stress magnitude.

4.3. Study limitations

There are several study limitation and assumptions that would need to be addressed. Although the BMHV's leaflets were modelled with linear elastic material and their motions were predicted by FSI coupling, the arterial wall was assumed to be rigid without blood vessel compliance. The rigid arterial wall assumption was made not only because of the PIV experimental validations but also served as a study control to isolate the influence of hematocrit in the analysis. Arterial wall compliance would be added as a future extension of the current study for investigating the significance of blood's shear thinning behaviour around the aortic valve. Additionally, since the current simulation was validated using similar validation procedure by the FDA with the use of Newtonian fluid for both the PIV experiment and the simulation [50], the verification of the non-Newtonian simulations could be further conducted experimentally using a shear-thinning blood analog that contains Xanthan gum [51]. Additionally, the hinges in our modelled BMHV were geometrically simplified without applied friction, this simplification was made because the microflow near the leaflet hinges as well as the hinge structural integrity was not the focus in the current study. Finally, the resolution artifact near wall from the PIV prevented accurate near-wall velocity measurements. It is planned to decrease the influence of the artifact by enhancing near-wall treatment as well as decrease seeding particle diameter.

5. Conclusion

We have constructed FSI models for simulating the hemodynamics

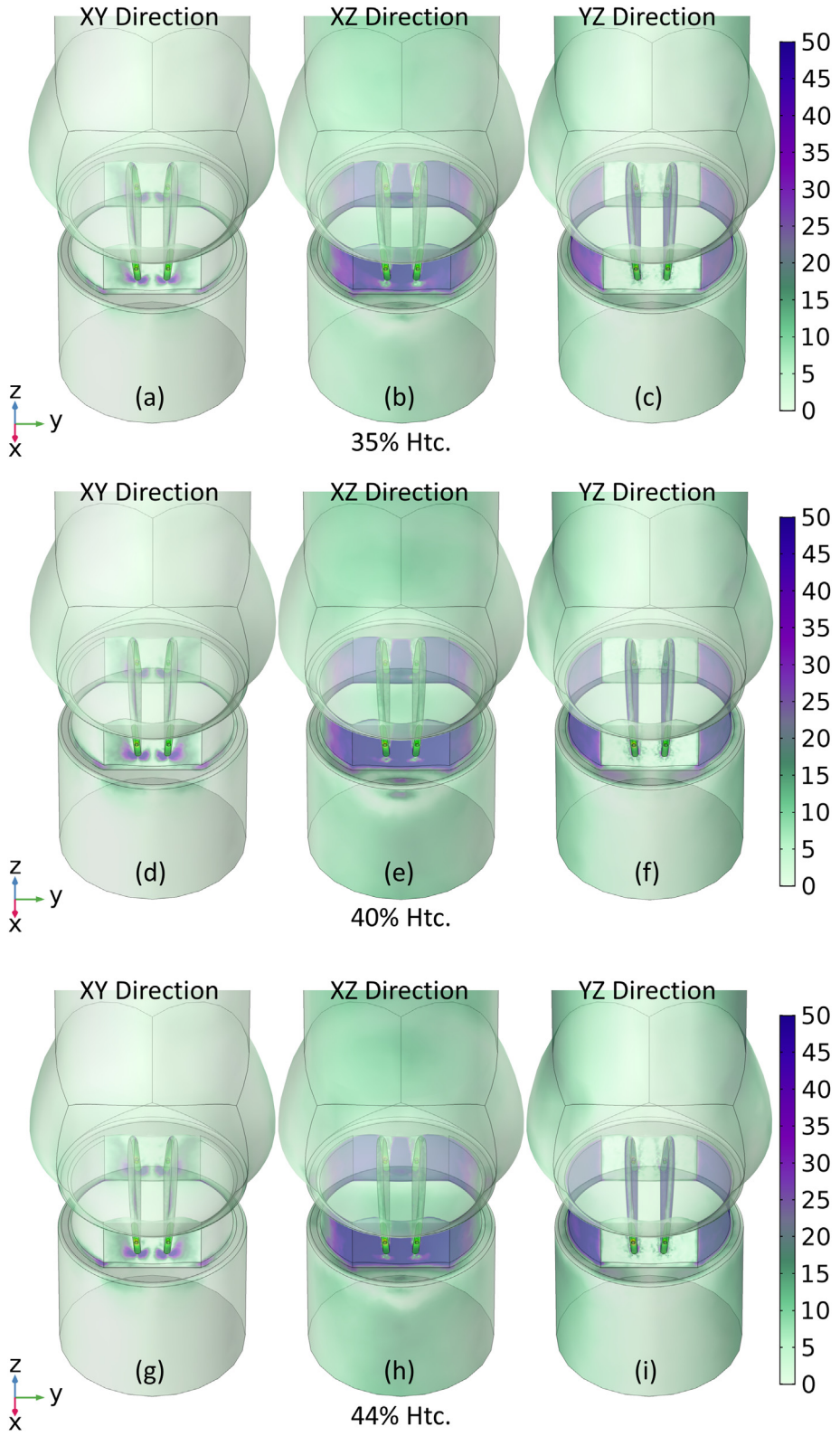

Fig. 14. 3D shear stress distribution in dPa (dyne/cm^2) at peak systolic phase for 35% Htc. (a, b, c), 40% Htc. (d, e, f), and 44% Htc. (g, h, i).

of BMHV with experimental validations using PIV measurements excluding the near wall measurement. The measurement near the test chamber wall had some noticeable uncertainties, due to optical artifact and seeding particle size. Therefore, we had to qualitatively verify our simulated results with literature published experimental results. Three models were built with the integration of the shear thinning Quemada model, which contained hematocrit as the controlling parameter. The fully-coupled FSI approach used in the current study successfully predicted the hemodynamics and leaflet motion of a BMHV. The inclusion of hematocrit as an additional modelling parameter could provide customized and personalized clinical assessments. The shear stress distribution, on the other hand, had a significant decrease with the

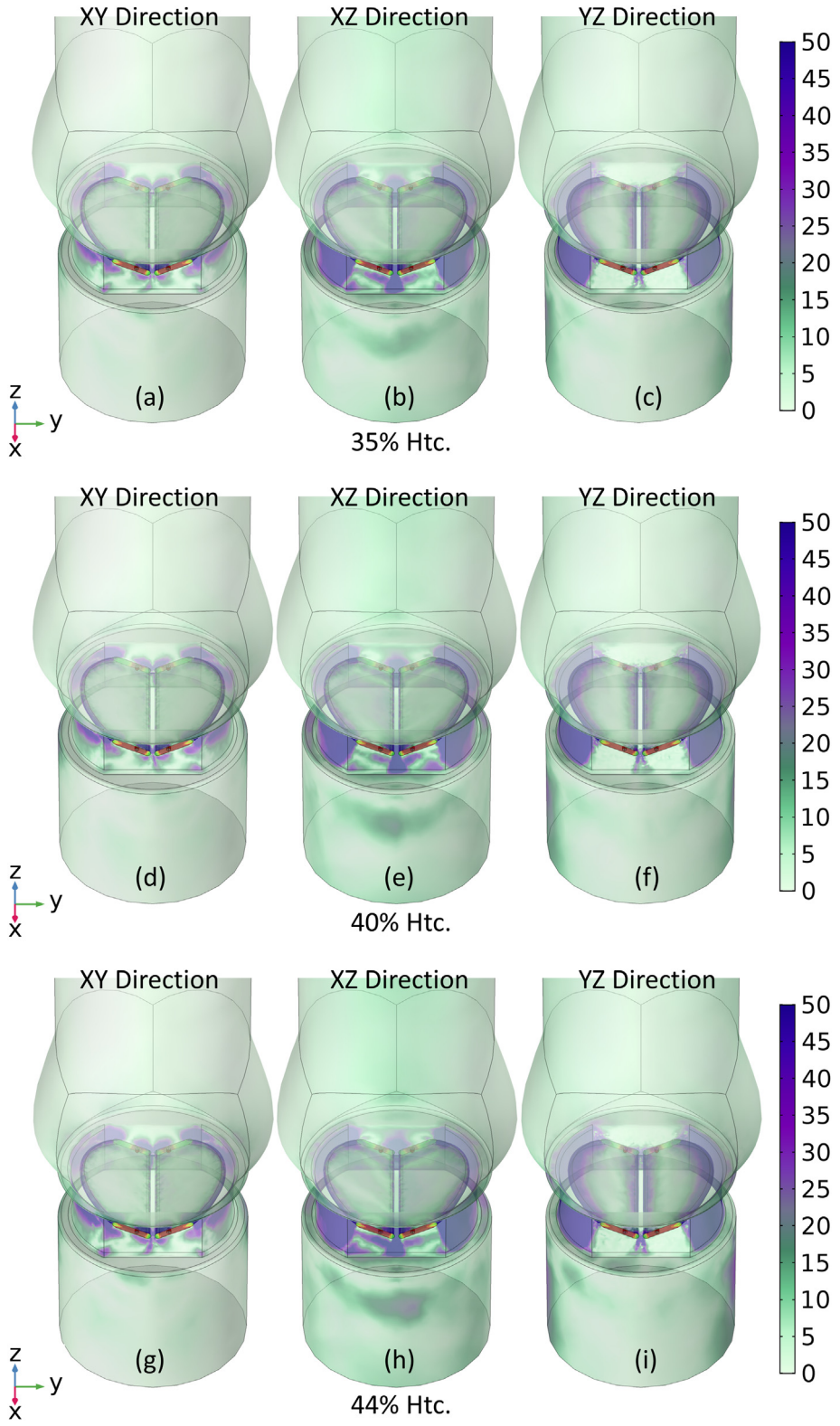

Fig. 15. 3D shear stress distribution in dPa (dyne/cm^2) at end diastolic phase for 35% Htc. (a, b, c), 40% Htc. (d, e, f), and 44% Htc. (g, h, i).

decrease in hematocrit. Our results suggested that the distributions of high shear stress during systole were around the valve leaflet surface and housing while during diastole were around the valve housing and the tips of the valve leaflet. Finally, the motion of valve leaflet was affected by the change in hematocrit with the most unstable opening for the lowest hematocrit at 35%. It was found that there was a hematocrit dependence on the hemodynamics of BMHV; therefore, it is important and critical to consider the impact of hematocrit when conducting patient-specific modelling.

Conflicts of interest

Oleksandr Barannyk is a former employee of ViVitro Labs Inc. All other authors declare that they have no conflict of interest.

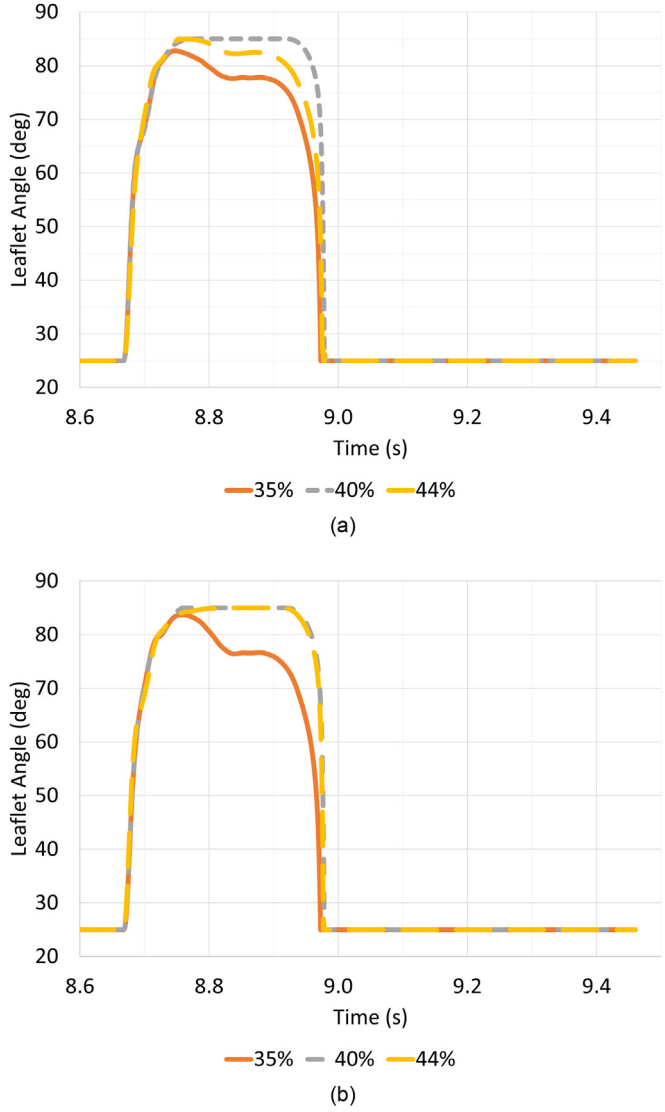

Fig. 16. Opening angle for the mechanical valve leaflets during one cardiac cycle.

Table 1
Summary of key parameters comparisons between the 35% Htc. case to 40% and 44% Htc. cases.

	35% Htc.	40% Htc.	44% Htc.
Shear Stress			
Max Shear Stress Magnitude (dPa)	1766	1935	2698
Difference in Max Shear Stress (%)		9.5%	52.7%
Time Averaged Shear Stress (dPa)	1006	1061	1437
Time averaged shear stress difference (%)		5.4%	42.8%
Leaflet Motion, Leaflet 1 (Leaflet 2)			
Max opening at (s)	8.747 (8.758)	8.762 (8.762)	8.754 (8.815)
Min closing at (s)	8.973 (8.973)	8.979 (8.978)	8.977 (8.977)
Opening duration (ms)	226 (214)	217 (217)	224 (162)
Leaflet Stress			
Max leaflet stress (MPa)	72.9	88.0	85.5
Difference in max leaflet stress (%)		20.7%	17.2%
Time-averaged difference (%)		11.7%	17.3%

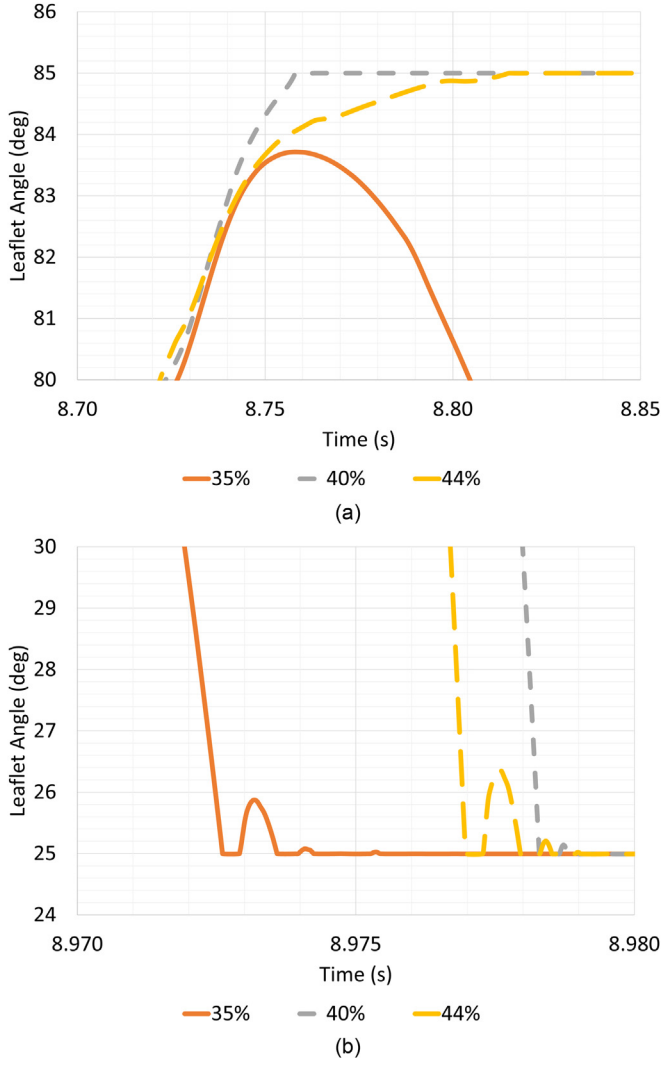

Fig. 17. Close-up view at the leaflet motion for Leaflet 2 at (a) peak opening and (b) initial closure.

Acknowledgment

The financial support of the Natural Sciences and Engineering Research Council (NSERC) of Canada is gratefully acknowledged. This research was enabled in part by the support provided by WestGrid (www.westgrid.ca) and Compute Canada (www.computecanada.ca).

Appendix A. Supplementary data

Supplementary data to this article can be found online at https://doi.org/10.1016/j.compbiomed.2019.05.003.

References

[1] D.A. McDonald, Blood Flow in Arteries, 2nd, UK Edward Arnold, London, 1974.
[2] B. Iung, G. Baron, E.G. Butchart, F. Delahaye, C. Gohlke-Bärwolf, O.W. Levang, P. Tornos, J.-L. Vanoverschelde, F. Vermeer, E. Boersma, P. Ravaud, A. Vahanian, A prospective survey of patients with valvular heart disease in europe: the euro heart survey on valvular heart disease, Eur. Heart J. 24 (2003) 1231–1243, https://doi.org/10.1016/S0195-668X(03)00201-X.
[3] A.P. Yoganathan, Z. He, S. Casey Jones, Fluid mechanics of heart valves, Annu. Rev. Biomed. Eng. 6 (2004) 331–362, https://doi.org/10.1146/annurev.bioeng.6.040803.140111.
[4] R.A. Nishimura, C.M. Otto, R.O. Bonow, B.A. Carabello, J.P. Erwin, L.A. Fleisher, H. Jneid, M.J. Mack, C.J. McLeod, P.T. O'Gara, V.H. Rigolin, T.M. Sundt, A. Thompson, 2017 AHA/ACC focused update of the 2014 AHA/ACC guideline for the management of patients with valvular heart disease: a report of the American

College of Cardiology/American heart association task force on clinical practice guidelines, Circulation 135 (2017) e1159–e1195, https://doi.org/10.1161/CIR.0000000000000503.
[5] M.N. Tillquist, T.M. Maddox, Cardiac crossroads: deciding between mechanical or bioprosthetic heart valve replacement, Patient Prefer. Adherence 5 (2011) 91–99, https://doi.org/10.2147/PPA.S16420.
[6] R. Halevi, A. Hamdan, G. Marom, K. Lavon, S. Ben-Zekry, E. Raanani, D. Bluestein, R. Haj-Ali, Fluid–structure interaction modeling of calcific aortic valve disease using patient-specific three-dimensional calcification scans, Med. Biol. Eng. Comput. 54 (2016) 1683–1694, https://doi.org/10.1007/s11517-016-1458-0.
[7] F. Piatti, F. Sturla, G. Marom, J. Sheriff, T.E. Claiborne, M.J. Slepian, A. Redaelli, D. Bluestein, Hemodynamic and thrombogenic analysis of a trileaflet polymeric valve using a fluid–structure interaction approach, J. Biomech. 48 (2015) 3641–3649, https://doi.org/10.1016/J.JBIOMECH.2015.08.009.
[8] B.M. Yun, L.P. Dasi, C.K. Aidun, A.P. Yoganathan, Computational modelling of flow through prosthetic heart valves using the entropic lattice-Boltzmann method, J. Fluid Mech. 743 (2014) 170–201, https://doi.org/10.1017/jfm.2014.54.
[9] G. Luraghi, W. Wu, F. DeGaetano, J.F. Rodriguez Matas, G.D. Moggridge, M. Serrani, J. Stasiak, M.L. Costantino, F. Migliavacca, Evaluation of an aortic valve prosthesis: fluid-structure interaction or structural simulation? J. Biomech. 58 (2017) 45–51, https://doi.org/10.1016/J.JBIOMECH.2017.04.004.
[10] L.P. Dasi, L. Ge, H.A. Simon, F. Sotiropoulos, A.P. Yoganathan, Vorticity dynamics of a bileaflet mechanical heart valve in an axisymmetric aorta, Phys. Fluids 19 (2007) 067105, , https://doi.org/10.1063/1.2743261.
[11] P. Youssefi, A. Gomez, T. He, L. Anderson, N. Bunce, R. Sharma, C.A. Figueroa, M. Jahangiri, Patient-specific computational fluid dynamics—assessment of aortic hemodynamics in a spectrum of aortic valve pathologies, J. Thorac. Cardiovasc. Surg. 153 (2017) 8–20, https://doi.org/10.1016/J.JTCVS.2016.09.040 e3.
[12] C. Guivier, V. Deplano, P. Pibarot, New insights into the assessment of the prosthetic valve performance in the presence of subaortic stenosis through a fluid-structure interaction model, J. Biomech. 40 (2007) 2283–2290, https://doi.org/10.1016/j.jbiomech.2006.10.010.
[13] K. Dumont, J.M.A. Stijnen, J. Vierendeels, F.N. van deVosse, P.R. Verdonck, Validation of a fluid–structure interaction model of a heart valve using the dynamic mesh method in fluent, comput, Methods Biomech. Biomed. Engin. 7 (2004) 139–146, https://doi.org/10.1080/10255840410001715222.
[14] A. Redaelli, H. Bothorel, E. Votta, M. Soncini, U. Morbiducci, C. DelGaudio, A. Balducci, M. Grigioni, 3-D simulation of the St. Jude Medical bileaflet valve opening process: fluid-structure interaction study and experimental validation, J. Heart Valve Dis. 13 (2004) 804–813.
[15] R. Cheng, Y.G. Lai, K.B. Chandran, Three-Dimensional fluid-structure interaction simulation of bileaflet mechanical heart valve flow dynamics, Ann. Biomed. Eng. 32 (2004) 1471–1483, https://doi.org/10.1114/B:ABME.0000049032.51742.10.
[16] I. Borazjani, L. Ge, F. Sotiropoulos, High-resolution fluid–structure interaction simulations of flow through a Bi-leaflet mechanical heart valve in an anatomic aorta, Ann. Biomed. Eng. 38 (2010) 326–344, https://doi.org/10.1007/s10439-009-9807-x.
[17] K. Dumont, J. Vierendeels, R. Kaminsky, G. vanNooten, P. Verdonck, D. Bluestein, Comparison of the hemodynamic and thrombogenic performance of two bileaflet mechanical heart valves using a CFD/FSI model, J. Biomech. Eng. 129 (2007) 558–565, https://doi.org/10.1115/1.2746378.
[18] C.R. Choi, C.N. Kim, Numerical analysis on the hemodynamics and leaflet dynamics in a bileaflet mechanical heart valve using a fluid-structure interaction method, Am. Soc. Artif. Intern. Organs J. 55 (2009) 428–437, https://doi.org/10.1097/MAT.0b013e3181b58f98.
[19] M. Nobili, U. Morbiducci, R. Ponzini, C. DelGaudio, A. Balducci, M. Grigioni, F. Maria Montevecchi, A. Redaelli, Numerical simulation of the dynamics of a bileaflet prosthetic heart valve using a fluid-structure interaction approach, J. Biomech. 41 (2008) 2539–2550, https://doi.org/10.1016/j.jbiomech.2008.05.004.
[20] T. HONG, C.N. KIM, A numerical analysis of the blood flow around the Bileaflet Mechanical Heart Valves with different rotational implantation angles, J. Hydrodyn. Ser. B. 23 (2011) 607–614, https://doi.org/10.1016/S1001-6058(10)60156-4.
[21] M. Krafczyk, M. Cerrolaza, M. Schulz, E. Rank, Analysis of 3D transient blood flow passing through an artificial aortic valve by Lattice-Boltzmann methods, J. Biomech. 31 (1998) 453–462, https://doi.org/10.1016/S0021-9290(98)00036-0.
[22] C. Guivier-Curien, V. Deplano, E. Bertrand, Validation of a numerical 3-D fluid—structure interaction model for a prosthetic valve based on experimental PIV measurements, Med. Eng. Phys. 31 (2009) 986–993, https://doi.org/10.1016/j.medengphy.2009.05.012.
[23] F. DeVita, M.D. deTullio, R. Verzicco, Numerical simulation of the non-Newtonian blood flow through a mechanical aortic valve, Theor. Comput. Fluid Dynam. 30 (2016) 129–138, https://doi.org/10.1007/s00162-015-0369-2.
[24] P. Hanafizadeh, N. Mirkhani, M.R. Davoudi, M. Masouminia, K. Sadeghy, Non-Newtonian blood flow simulation of diastolic phase in bileaflet mechanical heart valve implanted in a realistic aortic root containing coronary arteries, Artif. Organs 40 (2016) E179–E191, https://doi.org/10.1111/aor.12787.
[25] S.N. Doost, L. Zhong, B. Su, Y.S. Morsi, The numerical analysis of non-Newtonian blood flow in human patient-specific left ventricle, Comput. Methods Progr. Biomed. 127 (2016) 232–247, https://doi.org/10.1016/J.CMPB.2015.12.020.
[26] S.F.C. Stewart, E.G. Paterson, G.W. Burgreen, P. Hariharan, M. Giarra, V. Reddy, S.W. Day, K.B. Manning, S. Deutsch, M.R. Berman, M.R. Myers, R.A. Malinauskas, Assessment of CFD performance in simulations of an idealized medical device: results of FDA's first computational interlaboratory study, Cardiovasc. Eng. Technol. 3 (2012) 139–160, https://doi.org/10.1007/s13239-012-0087-5.
[27] S. Karimi, M. Dabagh, P. Vasava, M. Dadvar, B. Dabir, P. Jalali, Effect of rheological models on the hemodynamics within human aorta: CFD study on CT image-based geometry, J. Nonnewton. Fluid Mech. 207 (2014) 42–52, https://doi.org/10.1016/J.JNNFM.2014.03.007.
[28] D. Quemada, Rheology of concentrated disperse systems III. General features of the proposed non-Newtonian model. Comparison with experimental data, Rheol. Acta 17 (1978) 643–653, https://doi.org/10.1007/BF01522037.
[29] A. Marcinkowska-Gapińska, J. Gapinski, W. Elikowski, F. Jaroszyk, L. Kubisz, Comparison of three rheological models of shear flow behavior studied on blood samples from post-infarction patients, Med. Biol. Eng. Comput. 45 (2007) 837–844, https://doi.org/10.1007/s11517-007-0236-4.
[30] Z. Li, C. Kleinstreuer, Analysis of biomechanical factors affecting stent-graft migration in an abdominal aortic aneurysm model, J. Biomech. 39 (2006) 2264–2273, https://doi.org/10.1016/J.JBIOMECH.2005.07.010.
[31] J.R. Buchanan, C. Kleinstreuer, S. Hyun, G.A. Truskey, Hemodynamics simulation and identification of susceptible sites of atherosclerotic lesion formation in a model abdominal aorta, J. Biomech. 36 (2003) 1185–1196, https://doi.org/10.1016/S0021-9290(03)00088-5.
[32] L. Prahl Wittberg, S. vanWyk, L. Fuchs, E. Gutmark, P. Backeljauw, I. Gutmark-Little, Effects of aortic irregularities on blood flow, Biomechanics Model. Mechanobiol. 15 (2016) 345–360, https://doi.org/10.1007/s10237-015-0692-y.
[33] J. Novosadová, The changes in hematocrit, hemoglobin, plasma volume and proteins during and after different types of exercise, Eur. J. Appl. Physiol. Occup. Physiol. 36 (1977) 223–230.
[34] ISO 5840-2:2015, Cardiovascular Implants – Cardiac Valve Prostheses – Part 2: Surgically Implanted Heart Valve Substitutes (n.d.), https://www.iso.org/standard/51314.html.
[35] M. Raffel, C. Willert, S. Wereley, J. Kompenhans, Particle Image Velocimetry: A Practical Guide, Springer, 2007, https://doi.org/10.1007/978-3-540-72308-0_2.
[36] H. Huang, D. Dabiri, M. Gharib, On errors of digital particle image velocimetry, Meas. Sci. Technol. 8 (1997) 1427–1440, https://doi.org/10.1088/0957-0233/8/12/007.
[37] J. Westerweel, D. Dabiri, M. Gharib, The effect of a discrete window offset on the accuracy of cross-correlation analysis of digital PIV recordings, Exp. Fluid 23 (1997) 20–28, https://doi.org/10.1007/s003480050082.
[38] J. Westerweel, Fundamentals of digital particle image velocimetry, Meas. Sci. Technol. 8 (1997) 1379–1392, https://doi.org/10.1088/0957-0233/8/12/002.
[39] V.-T. Nguyen, Y.H. Kuan, P.-Y. Chen, L. Ge, F. Sotiropoulos, A.P. Yoganathan, H.L. Leo, Experimentally validated hemodynamics simulations of mechanical heart valves in three dimensions, Cardiovasc. Eng. Technol. 3 (2012) 88–100, https://doi.org/10.1007/s13239-011-0077-z.
[40] C.-P. Li, C.-W. Lo, P.-C. Lu, Estimation of viscous dissipative stresses induced by a mechanical heart valve using PIV data, Ann. Biomed. Eng. 38 (2010) 903–916, https://doi.org/10.1007/s10439-009-9867-y.
[41] M. OHMI, M. IGUCHI, Critical Reynolds number in an oscillating pipe flow, Bull. JSME. 25 (1982) 165–172, https://doi.org/10.1299/jsme1958.25.165.
[42] K. Sriram, M. Intaglietta, D.M. Tartakovsky, Non-Newtonian flow of blood in arterioles: consequences for wall shear stress measurements, Microcirculation 21 (2014) 628–639, https://doi.org/10.1111/micc.12141.
[43] H.H. Yeh, D. Grecov, S. Karri, Computational modelling of bileaflet mechanical valves using fluid-structure interaction approach, J. Med. Biol. Eng. 34 (2014) 482–486, https://doi.org/10.5405/jmbe.1699.
[44] H.H. Yeh, S.W. Rabkin, D. Grecov, Hemodynamic assessments of the ascending thoracic aortic aneurysm using fluid-structure interaction approach, Med. Biol. Eng. Comput. 56 (2018) 435–451, https://doi.org/10.1007/s11517-017-1693-z.
[45] H.A. Simon, L. Ge, F. Sotiropoulos, A.P. Yoganathan, Simulation of the three-dimensional hinge flow fields of a bileaflet mechanical heart valve under aortic conditions, Ann. Biomed. Eng. 38 (2010) 841–853, https://doi.org/10.1007/s10439-009-9857-0.
[46] K. Yu, P. Andruschak, H.H. Yeh, D. Grecov, J.N. Kizhakkedathu, Influence of dynamic flow conditions on adsorbed plasma protein corona and surface-induced thrombus generation on antifouling brushes, Biomaterials 166 (2018) 79–95, https://doi.org/10.1016/j.biomaterials.2018.03.009.
[47] P. Ternik, Planar sudden symmetric expansion flows and bifurcation phenomena of purely viscous shear-thinning fluids, J. Nonnewton. Fluid Mech. 157 (2009) 15–25, https://doi.org/10.1016/J.JNNFM.2008.09.002.
[48] K.K. Yeleswarapu, J.F. Antaki, M.V. Kameneva, K.R. Rajagopal, A mathematical model for shear-induced hemolysis, Artif. Organs 19 (1995) 576–582, https://doi.org/10.1111/j.1525-1594.1995.tb02384.x.
[49] S.C. Cannegieter, F.R. Rosendaal, A.R. Wintzen, F.J.M. van derMeer, J.P. Vandenbroucke, E. Briet, Optimal oral anticoagulant therapy in patients with mechanical heart valves, N. Engl. J. Med. 333 (1995) 11–17, https://doi.org/10.1056/NEJM199507063330103.
[50] R.A. Malinauskas, P. Hariharan, S.W. Day, L.H. Herbertson, M. Buesen, U. Steinseifer, K.I. Aycock, B.C. Good, S. Deutsch, K.B. Manning, B.A. Craven, FDA benchmark medical device flow models for CFD validation, Am. Soc. Artif. Intern. Organs J. 63 (2017) 150–160, https://doi.org/10.1097/MAT.0000000000000499.
[51] L. Campo-Deaño, R.P.A. Dullens, D.G.A.L. Aarts, F.T. Pinho, M.S.N. Oliveira, Viscoelasticity of blood and viscoelastic blood analogues for use in polydymethylsiloxane *in vitro* models of the circulatory system, Biomicrofluidics 7 (2013) 034102, , https://doi.org/10.1063/1.4804649.